Aerodynamics of Boundary Layer Ingesting Fuselage Fans

Alejandro Castillo Pardo*, Cesare A. Hall
ac2181@cam.ac.uk

Whittle Laboratory
University of Cambridge
Cambridge
United Kingdom

ABSTRACT

Boundary Layer Ingestion (BLI) potentially offers a large reduction in fuel burn and pollutant emissions. The Propulsive Fuselage Concept features an electrically driven fan at the aft section of the airframe that ingests 360° of the fuselage boundary layer. As a result, the distortion at the fan face during cruise is reduced to radial. This paper aims to devise and test a fan design philosophy that is tuned to this inflow distortion.

Initially a free-vortex fan design is presented, which is matched to clean, undistorted inflow. The effects of fuselage BLI on the aerodynamics of this fan are investigated. A series of design steps are then presented to develop the free-vortex fan into a new design that is matched to fuselage BLI conditions. Both fan designs have been manufactured and tested within a low speed rig that can make high-resolution flow field measurements. The measured aerodynamics of both fans operating with BLI-type distortion are compared with computational results. The impact of the fan design changes on the aerodynamics and the performance with BLI are evaluated using the test results.

This paper presents the successful application of a unique experimental facility for the analysis of BLI fuselage fans. It shows that it is possible to design a fan that accepts the radial distortion caused by fuselage BLI with a modified profile of work input. The test results demonstrate that such a fan can be designed for fuselage BLI that gives increased work input and pressure rise relative to a fan designed for clean flow. The new fan design presented has reduced loading near the hub to account for the incoming distortion, increased mid span loading and negative incidence towards the tip for tolerance to circumferential distortion off-design.

Keywords: Aerodynamics; Fan; Boundary Layer Ingestion; Propulsion; Inlet Flow Distortion

* Corresponding author

1.0 INTRODUCTION

The CENTRELINE project [1] aims to demonstrate the propulsive fuselage aircraft concept illustrated in Fig. 1. This configuration features an electrically driven fan at the aft of the airframe that ingests 360° of the fuselage boundary layer. Consequently, the distortion at the fan face during cruise is essentially radial, whereas other Boundary Layer Ingestion (BLI) installations [2, 3] create a highly mixed circumferential and radial distortion. It should therefore be possible to minimise any losses in fan efficiency and stability margin due to BLI through a new design approach that counteracts the distorted inflow.

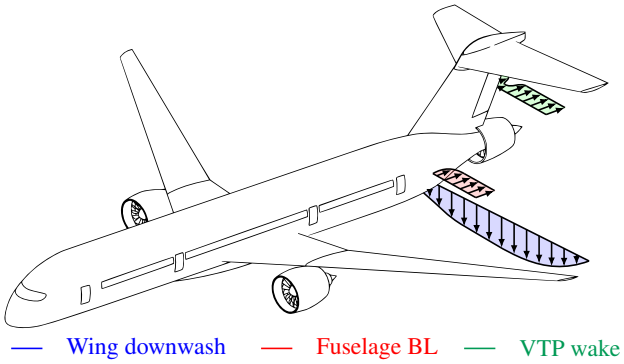

Figure 1. Sketch of sources of distortion at the inlet of the fuselage fan. Adapted from Seitz *et al.* [1].

There have been relatively few previous studies of the effects of radial distortion on fan aerodynamics and design. NASA tests in the 1970s with and without radial distortion [4–6] demonstrated how within a distorted region (an area of low total pressure) the rotor incidence angles are locally increased, loading up the blade sections and increasing the work input. It was noted how regions of high diffusion factor generally corresponded to high loss coefficient. The results also indicated how flow radially redistributes as a result of distortion, with mass flow migrating from regions of high total pressure towards low total pressure. This radial redistribution in mass flow was also described in detail in [7], for a mixed circumferential and radial distortion. In this case, the radial flow non-uniformity was reduced upstream and within a fan rotor. The redistribution was found to modify the rotor incidence and work variation.

The inflow of interest for a BLI fuselage fan at cruise is a severe and continuous hub-low radial distortion. This would normally tend to load up the inner sections of the rotor, leading to possible flow separation, combined with reduced loading towards the tip. This would be expected to reduce both fan efficiency and pressure ratio as shown in [4, 5]. However, an improved radial loading distribution is possible if the rotor is carefully designed to accept the non-uniform inflow. At each spanwise location, the blades can be optimally aligned with the inflow and loaded such that they give the required work input whilst also remaining efficient. This paper aims to devise such a design philosophy for fuselage fans and to demonstrate it experimentally.

The paper starts by presenting the computational methods used for the fan aerodynamic designs and the experimental methods used for the measurements. In the following design section a conventional, free-vortex style fan design, Fan A, is presented that satisfies the non-dimensional work and flow requirements of the fuselage fan at cruise. Fan A has been tested in clean and distorted conditions representative of fuselage BLI. A new design, Fan B, is then

Table 1
Design point parameters for the BLI fan rig.

Flow coefficient ϕ	0.69
Stage loading coefficient Ψ	0.44
Rotor inlet tip Mach number	0.16
Rotor tip Reynolds number	$2.1 \cdot 10^5$
Rotor hub-to-tip radii ratio	0.51
Running tip clearance (% span)	0.35
Number of rotor, stator blades	20, 30

presented that is improved from Fan A through a series of design steps for operation with fuselage. Experimental measurements of fan B operating within a boundary layer have been taken. Comparisons of the numerical methods and the experimental results are presented to validate the design approach. The effects of radial distortion on the flow field are examined by comparing the measured results in clean and distorted flow. The main results section presents the measured changes in the aerodynamics and performance between Fan B and Fan A when operating within distorted flow.

This paper shows that it is possible to design a fan stage for fuselage BLI that gives improved efficiency and pressure rise relative to a conventional design. The measured results are encouraging as they demonstrate that a fuselage fan operating in distorted flow can deliver the required performance with marginal loss compared to a fan designed for clean flow operating in clean flow. The paper should be of interest to researchers working in the field of BLI engines and fan-distortion interaction.

2.0 EXPERIMENTAL AND COMPUTATIONAL METHODS

Experimental methods

The experimental rig used for this research is a low-speed single-stage fan, known as the BLI rig. This facility was originally built by Gunn *et al.* [7–9] for the analysis of low hub-to-tip radii ratio BLI fan aerodynamics. It has been updated substantially for this research to study the aerodynamics of aft-section BLI fuselage fans.

Figure 2 presents the meridional view of the updated BLI fan rig. The rig is equipped with a long intake duct which enables the free interaction of the incoming distorted flow with the rotor. The annulus geometry has been modified to match the hub-to-tip radii ratio of the aft-section fan. Additionally, new rotor and OGV blades have been fitted into the rig. The low-speed nature of the rig does not allow full-scale compressibility effects to be replicated. Nevertheless, velocity triangles representative of the full-scale transonic aft-section fuselage fan are reproduced by matching the full-scale design flow coefficient and stage loading coefficient presented in Table 1.

Detailed pressure measurements were carried out at five axial stations with a five-hole pneumatic probe area traverse system. The five-hole probe measured the time-average values of stagnation pressure, static pressure, swirl flow angle, and radial flow angle. Based on these properties and the incompressibility of the flow, the velocity field, work input, and loss sources

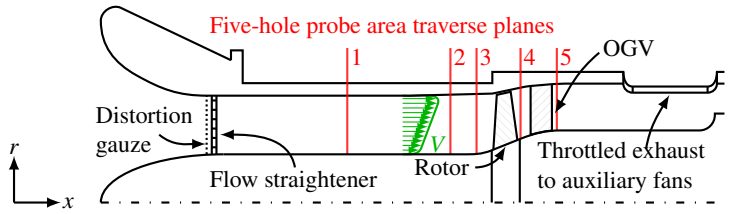

Figure 2. Meridional view of the BLI fan rig indicating measurement stations, to scale.

were fully resolved. The probe was calibrated over a range of yaw and pitch angles between +35° and +35° using the procedure reported in [10]. The pressure probe was traversed radially and azimuthally across 36 degree sectors at stations 1-5. Measurements were taken with a resolution of 25 radial and 37 circumferential positions at stations 1-4. The circumferential resolution was doubled downstream of the OGV, at station 5, to capture the blade wakes in greater detail.

Experimental tests have been carried out for clean and distorted inlet boundary conditions. The distortion chosen for this study is an axisymmetric but radially non-uniform profile of axial velocity and therefore stagnation pressure. This profile represents the boundary layer velocity profile found at the inlet highlight plane of CENTRELINE's aft propulsor at the design flow coefficient [1, 11]. Note that for this initial design phase of the project, the inflow is assumed to be purely axial and axisymmetric. Other sources of distortion have been neglected.

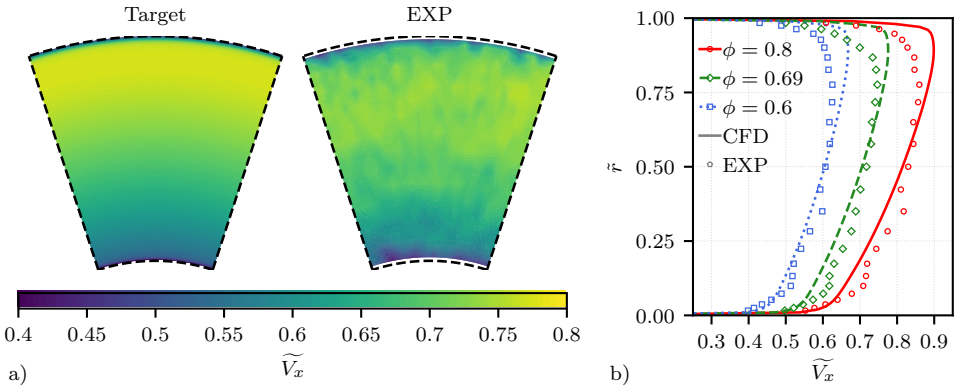

Figure 3. Inlet velocity profile: a) Comparison of target and measurements at design point, b) Radial profiles at different operating points.

A variable porosity distortion gauze was installed at the intake of the rig to generate the target inlet velocity profile. The distortion gauze was designed and 3D printed as a single sheet with a precisely controlled distribution of porosity [7]. The resultant inlet profile has been measured at station 1 to verify the effectiveness of the distortion gauze. Figure 3(a) presents the comparison between the target and the measured inlet boundary conditions. Good agreement is observed from 0% to 80% span. The agreement is degraded closer to the casing due to interaction between the inlet casing boundary layer and the gauze. Pitchwise average inlet velocity profiles derived for different operating points along the fan characteristic line are shown in Fig. 3(b).

Computational methods

Single-passage, steady-state simulations were carried out using the GPU-accelerated CFD code `Turbostream` [12]. `Turbostream` is a 3D, unsteady, Reynolds-averaged Navier Stokes solver running on structured multi-block meshes. The one-equation Spalart-Allmaras turbulence model [13] was used for all simulations along with adaptive wall functions and a y+ value of approximately 5 on all solid walls.

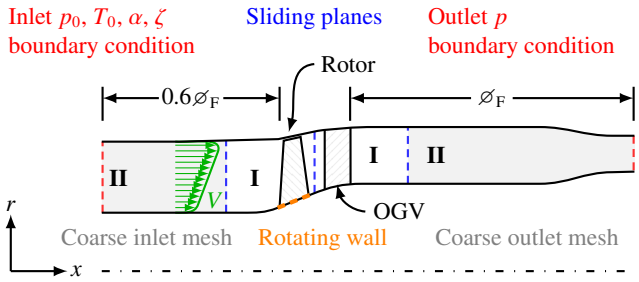

Figure 4. Meridional view of the BLI fan computational domain showing the fine (**I**) and coarse (**II**) mesh regions.

Figure 4 shows the meridional view of the computational domain, which is an accurate representation the experimental setup of the BLI rig. The domain was extended 0.6 diameter upstream and 1 diameter downstream of the fan stage to allow enough space for the fan-distortion interaction to take place. The inlet coincides with measurement station 1 and the CFD outlet was located at the rig exhaust. The structured multi-block computational mesh was generated using `NUMECA IGG/Autogrid5` [14]. The computational domain was split in two fine mesh regions (**I**) and two coarse mesh regions (**II**). Rotor and OGV blades were contained within (**I**) subdomains, which were characterised by an O4H topology with an O-mesh around each blade. In contrast, a H topology was used to mesh the inlet and outlet subdomains (**II**). Around 2.5 and 1.9 million nodes were used per rotor and OGV blade passage, respectively. Previous studies showed the suitability of this setup for the aerodynamic analysis of distortion ingesting fans [7, 15].

Radial distributions of stagnation pressure and flow angles were prescribed as inlet boundary conditions of the numerical model. Two types of simulations were run: clean and distorted. For clean flow cases uniform inlet flow conditions were applied. Any non-uniformity of the flow was contained within the hub and casing boundary layers. For distorted cases axisymmetric, but radially non-uniform profiles of stagnation pressure matching the target fuselage boundary layer were applied at the inlet of the domain. The operating point of the model was controlled by varying the static pressure specified at the outlet boundary of the convergent nozzle.

3.0 DESIGN OF AFT-SECTION FUSELAGE FANS

This section firstly describes the baseline fan design, fan A. It then explores how the incidence and work input for this fan are modified with BLI. This leads to the steps taken to obtain a new fan design, fan B, adjusted for the inlet distortion shown in Fig. 3. Note that both fan designs A and B are matched to the overall design parameters detailed in Table 1. Both designs also

use the same stator design, which was aligned to the exit flow angles from fan A operating in clean flow.

Fan A: Conventional free-vortex design

The rotor of fan A was designed to give a spanwise distribution of flow turning that produces approximately constant $\Delta h_0/U^2_{\text{mid}}$ as shown in Fig. 5(a) for clean conditions. The leading edge (LE) metal angle has been tailored to operate at minimum pressure loss incidence at the design point flow coefficient. The blade chord distribution was chosen to reduce Lieblein's Diusion Factor DF [16] to a value under 0.35 as presented in Fig. 5(b) for uniform inflow. It is noted that endwall effects lead to larger values of loading and DF at the hub and casing.

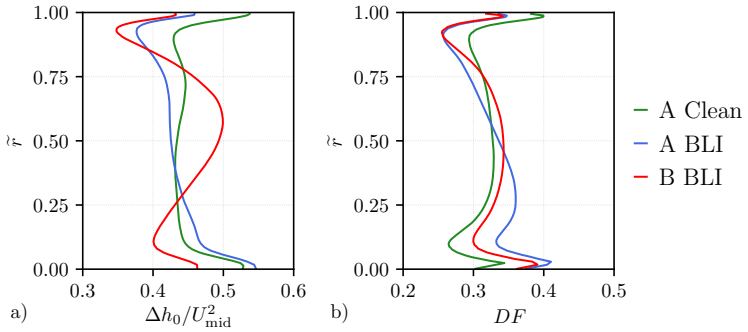

Figure 5. Computed spanwise distributions of: a) work loading and b) Lieblein's diffusion factor.

The effects of BLI on incidence and work input

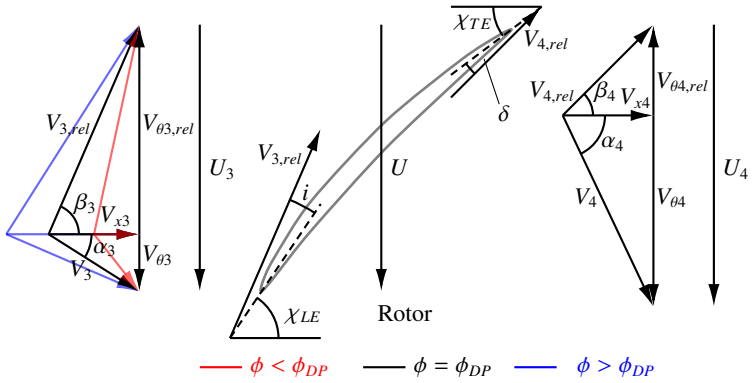

Figure 6. Rotor blade velocity triangle changes due to boundary layer ingestion.

Figure 6 is a velocity triangle sketch to illustrate the effects of flow coefficient changes due to fuselage BLI. When operating with distortion due to fuselage BLI, inner sections of the fan blade are subjected to an axial velocity deficit. The midspan region operates at the design conditions and the outer sections are at increased axial velocities. Consequently, the

region next to the hub operates at high incidence, while the tip sections of the blade operates at negative incidence. The effects of BLI on section incidence are observed in Fig. 7, where predicted changes in the pressure distributions are presented. The midspan section of fan A operates at design incidence even with the ingestion of a boundary layer. The hub loading is increased with BLI and operates at positive incidence. The tip moves towards negative incidence and reduced loading with BLI.

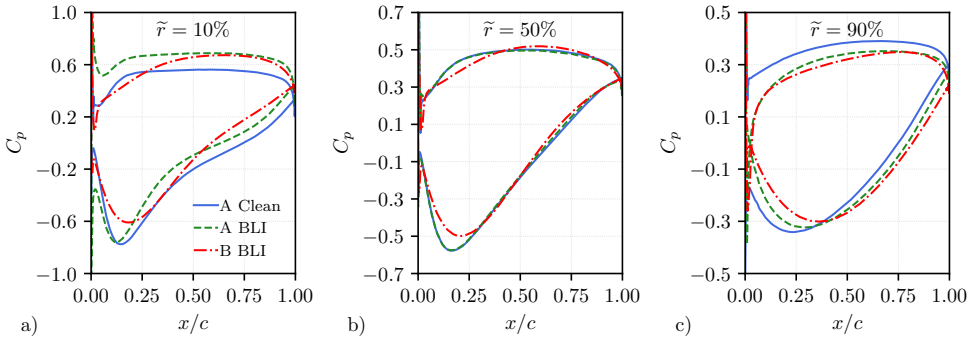

Figure 7. Pressure coefficient distributions of fan A and fan B in clean and BLI conditions - a) 10% span, b) 50% span, c) 90% span.

To evaluate the effect of radial distortion on the local loading, the Euler work equation (Eq. 1) can be non-dimensionalised, as shown by Eq. 2.

$$\Delta h_0 = U_4 V_{\theta 4} - U_3 V_{\theta 3} \qquad \ldots(1)$$

$$\Psi_3 = \frac{\Delta h_0}{U_3^2} = \frac{r_4^2}{r_3^2} + \frac{r_4}{r_3}\frac{\widetilde{V_{x4}}}{\widetilde{V_{x3}}}\widetilde{V_{x3}}\tan\beta_4 - \widetilde{V_{x3}}\tan\alpha_3 \qquad \ldots(2)$$

For this specific type of distortion it can be assumed axial flow ($\alpha_3 \approx 0.0$), minor modification of the streamtube thickness ($\Delta r_4/r_3 \ll \Delta\widetilde{V_{x3}}$, $\Delta\,(r_4/r_3)^2 \ll \Delta\widetilde{V_{x3}}$, $\Delta\widetilde{V_{x4}}/\widetilde{V_{x3}} \ll \Delta\widetilde{V_{x3}}$), and constant deviation $\Delta\tan\beta_4 \ll \Delta\widetilde{V_{x3}}$. Consequently, the dominant term on the local loading of the blade Ψ_3 is the local flow coefficient $\widetilde{V_{x3}}$. The deficit of axial velocity at the inner sections results in increased local loading and diffusion factors (since beta is negative). In contrast, the tip sections get unloaded due to the excess of axial velocity. These trends are illustrated in Fig. 5 by the computed changes in work input for fan A due to BLI. The large extent of the unloaded region towards the tip leads to the significant overall loss in stage loading coefficient observed in Fig. 8(a). The inability of the rotor to produce the design work input along with the off-design incidence results in a degradation of the isentropic efficiency of the rotor as presented in Fig. 8(b).

Fan B: Design for BLI distortion

Step 1: Realignment of the leading edge

Figure 7(a) and Fig. 7(b) show the pressure distribution of the 10% and 50% span section of fan B realigned for minimum loss with BLI distortion. At 10% span, the positive incidence

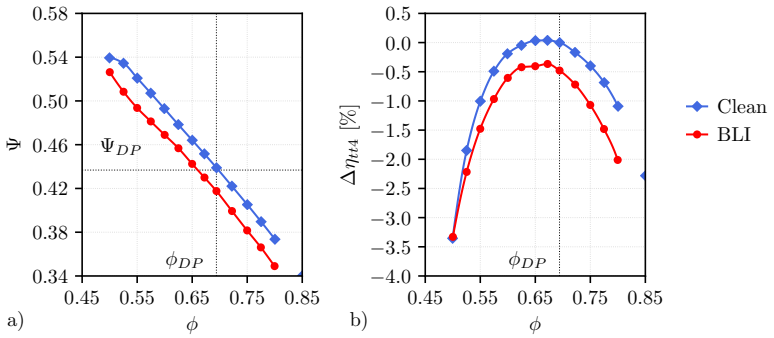

Figure 8. Effect of distortion ingestion on the computed A fan characteristics at constant rotor speed: a) stage loading, b) isentropic efficiency.

and section loading is significantly reduced. The incidence and loading have also been improved at midspan. Towards the tip, as shown by the 90% span section, the airfoil has been restaggered to operate at negative incidence at design point.

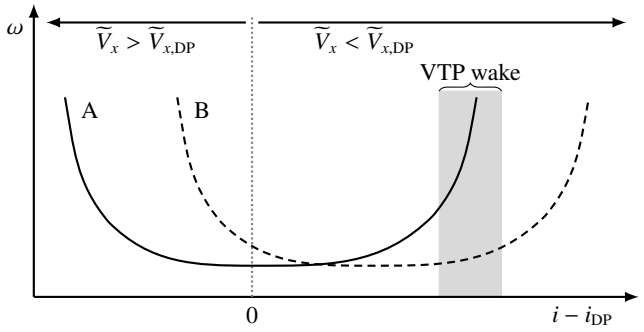

Figure 9. Sketch of airfoil loss loop.

Although the flow is assumed to be axisymmetric during the design phase, the fuselage fan needs to be tolerant to large incidence fluctuations such as the ones caused by the vertical tail plane (VTP) wake, Fig. 1. Figure 9 presents a sketch of typical loss bucket curves. When airfoil A operates at its design point incidence, the loss is minimum. For high values of negative or positive incidence the loss increases substantially. The shaded area illustrates the expected range of incidence found within a VTP wake. To increase the tolerance of the profile to such an event, airfoil B is shown, which is the same as A but restaggered to negative incidence. This section is expected to operate within the VTP wake without high loss or instability at the expense of reduced efficiency at design point. This approach was applied progressively from 75% span towards the tip to improve the distortion tolerance of the blade.

Step 2: Midspan blade loading

A radial distribution of work for fan B was chosen that produced a midspan loaded blade, as shown in Fig. 5(a). As shown above, the rotor hub work tends to be increased by BLI, leading to high hub diffusion factors and high angles into the stator. The tip of the blade can be sus-

ceptible to incidence excursions and needs to have good operability. A mid loaded blade was therefore chosen as this was expected to provide the required work input with good efficiency and stability. Once the sections next to the tip were restaggered for negative incidence, the amount of turning was reduced further to improve the tolerance to circumferential distortion. The inner sections were unloaded until the diffusion factor was reduced to acceptable levels (see below). Flow turning can be better perform in the mid span region, as there are no endwall effects and a small impact on the operation of the OGV is caused.

Step 3: Controlling the diffusion factor

The restaggering and recambering steps described above lead to a blade with high values of diffusion factor at midspan. To reduce the diffusion to acceptable values, the solidity was progressively increased from the hub to 50% span and progressively reduced to the original value at the tip. The final radial profiles of work and DF of fan B in BLI conditions are presented in Fig. 5. The radial distribution of blade LE and trailing edge metal angles are presented in Fig. 10(a). The corresponding solidity variation is detailed in Fig. 10(b). This shows the increase in solidity for fan B required to keep the diffusion factor below 0.35.

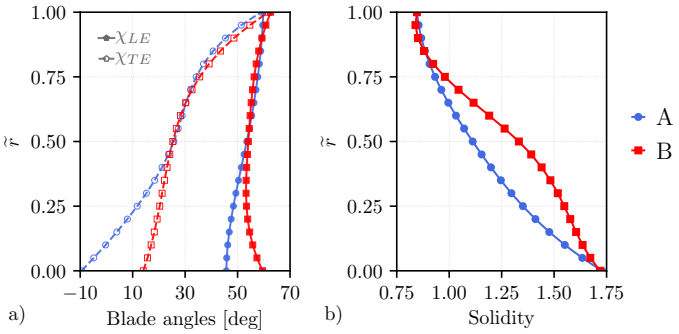

Figure 10. Rotor geometry.

Three blade sections for both fan A and fan B are shown in Fig. 11. The larger 50% span chord shown for design B in Fig. 11 is consistent with the increase in solidity shown in Fig. 10(b). Note that there has not been any detailed mechanical analyses of fan A or B, but to reduce the unsteady bending moments of the blade, the sections have been stacked radially on their centroids.

Predicted performance comparison

The comparison of the performance of fans A and B with BLI conditions is presented in Fig. 12. The capability of fan B to transfer work to the flow has been recovered, as shown in Fig. 12(a), satisfying the design point specification. The recovery of the lost pressure rise is carried out without penalising the total-to-total efficiency at the design point flow coefficient.

One of the key aspects targeted in the design of fan B was the capability to operate more efficiently off-design (towards stall). This has been done by unloading the tip and staggering the section with negative incidence at the design point. This approach is a compromise

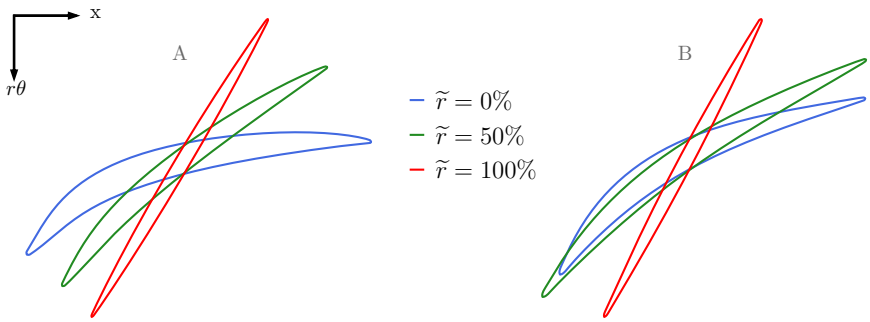

Figure 11. Rotor blade sections at 0, 50 and 100% span of fan A and fan B.

between maximising the design point efficiency and extending the operating range. The resulting total-to-total efficiency characteristic line is shown in Fig. 12(b). An offset of between 0.5% and 1.0% in efficiency is consistently found for lower flow coefficients.

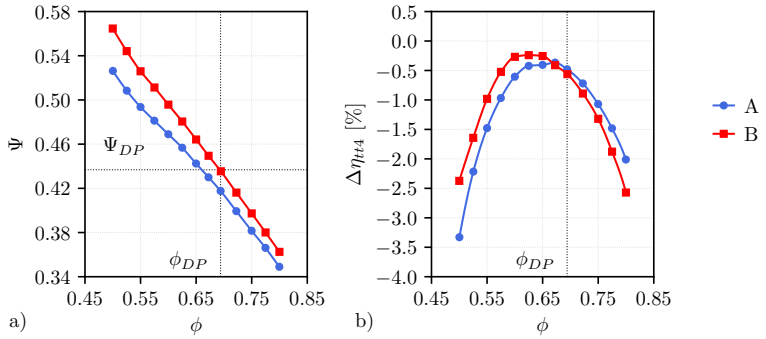

Figure 12. Comparison of computed A and B distorted fan characteristics at constant rotor speed. a) stage loading, b) isentropic efficiency.

4.0 RESULTS

Design approach validation

Figure 13 presents measured (symbols) and computed (lines) spanwise distributions at the fan face (s3), outlet of the rotor (s4) and donwstream of the OGV (s5) for fan A. The distortion gauze installed at the inlet of the rig aims to replicate CENTRELINE's target velocity profile. As it was shown in Fig. 3, the interaction of the gauze and the inlet casing boundary layer reduces the velocity attained between 80 and 100% span. The deficit of axial velocity propagates downstream and has been consistently measured at the fan face (Fig. 13(a)). Minor discrepancies between the target and the measurements have been found for other radial locations. The flow redistributes across the rotor, moving the location of maximum velocity to 70% span. Additional migration of flow towards lower parts of the span is identified. The flow further redistributes and becomes more homogeneous through the OGV. The mass flow redistribution is consistently captured with numerical and experimental techniques.

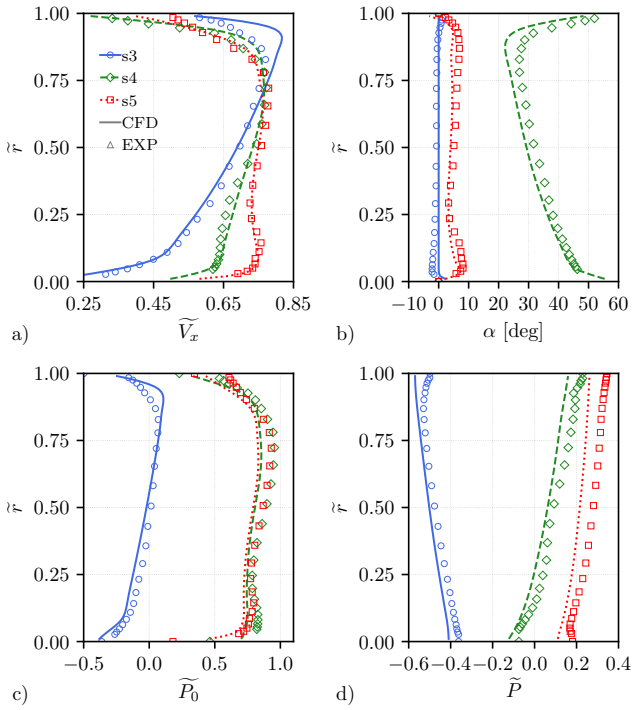

Figure 13. Measured (symbols) and computed (lines) spanwise distributions of fan A - a) axial velocity, b) absolute swirl angle, c) stagnation pressure, c) static pressure.

The discrepancy in velocity measured between 80 and 100% span causes the rotor blade to operate at a higher incidence and work input than in the numerical simulations, increasing the turning and pressure rise. The associated increase in flow turning is observed in terms of absolute swirl angle at s4 (Fig. 13(b)). There is very good agreement between experiments and CFD, with a small numerical underprediction of swirl angle. As a result, the stator blade is demanded to turn more the flow in the experiments, leading to increased deviation and swirl angle downstream of thestage.

The increased turning measured behind the rotor is directly translated into larger work input and pressure rise. This is confirmed in Fig. 13, where an offset between the computed and measured stagnation pressure is observed at s4 and s5. A similar offset is observed in Fig. 13 in terms of static pressure, which follows due to the good agreement shown in velocity.

The phenomena described above for fan A are observed in Fig. 14 for fan B. Good agreement between measurements and computations of axial velocity is found except in the 80-100% span region upstream of the fan. The discrepancy is associated to the velocity profile generated by the distortion gauze. A migration of the flow towards the mid span region is observed across the rotor and stator blades (Fig. 14(a)). The rotor blade is consistently able to generate more work in the experiments, leading to higher swirl angles at s4 and larger stator deviation (Fig. 14(b)). The increased turning measured behind the rotor offsets the stagnation pressure distribution towards higher values (Fig. 14(c)). An offset in static pressure is measured, which is consequence of the good agreement in axial velocity.

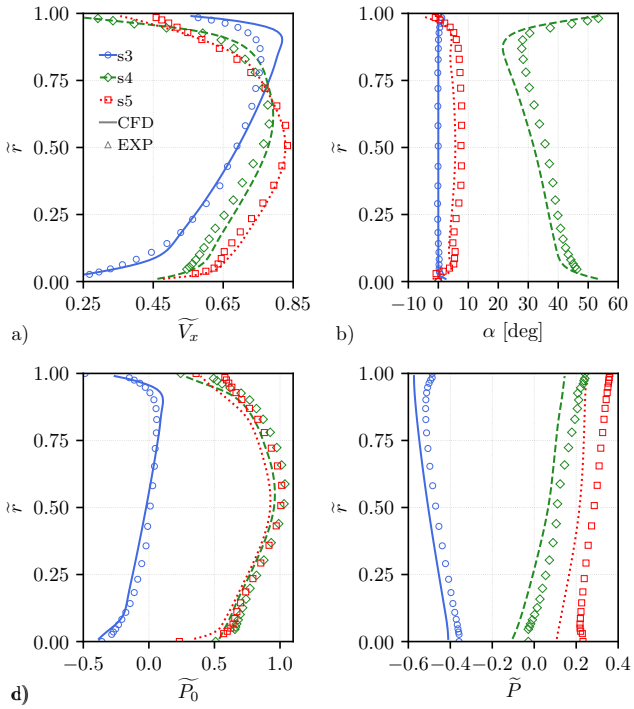

Figure 14. Measured (symbols) and computed (lines) spanwise distributions of fan B - a) axial velocity, b) absolute swirl angle, c) stagnation pressure, c) static pressure.

The agreement between numerical results and experimental measurements reinforces the confidence in the approach presented in Section 3, for the design of the BLI fuselage fan.

Impact of BLI on fan aerodynamics

Experiments with undistorted (clean) and distorted (BLI) inflows were performed with fan A. To operate at the same flow coefficient in both types of inflow, the deficit of axial velocity observed below 50% span at the fan face (Fig. 15(a)) is balanced by an excess of velocity above 50% span. The drop in radial angle at the fan face observed in Fig. 15(d) for the BLI case indicates a radial migration of flow towards the region of lower stagnation pressure upstream and through the rotor. Consequently, a more uniform distribution of axial velocity is found at s4 . Recalling the velocity triangles presented in Fig. 6, regions of low and high axial velocity are linked with areas of increased and reduced relative swirl angle respectively. This is illustrated in Fig. 15(b), where the changes in relative swirl angle at s3 are shown along with the respective LE metal angle. Therefore, the blade continuously operates at off-design incidence inside the fuselage boundary layer. The computed C_p distributions shown in Fig. 7 reaffirms the increased incidence found near the hub and the movement towards negative incidence near the tip.

In addition to variations in incidence, the amount of turning developed by the rotor blade changes as a results of BLI. Increased turning is observed in Fig. 15(c) below 50% span. The

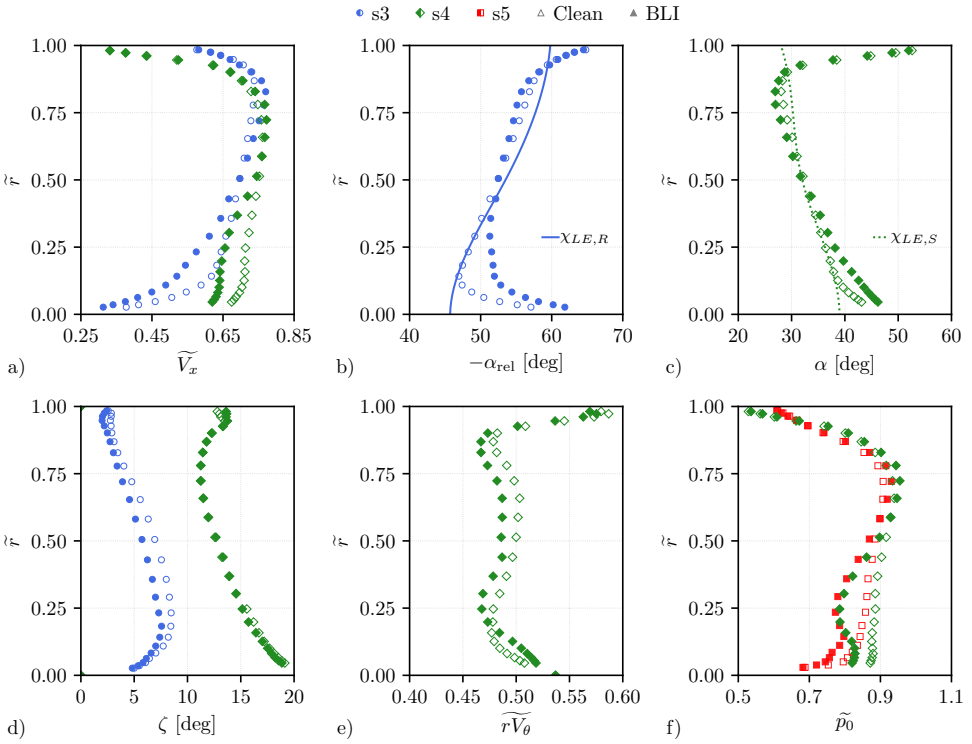

Figure 15. Measured spanwise distribution of fan A in clean and BLI flows - a) relative swirl angle, b) absolute swirl angle, c) radial angle, d) axial velocity, e) specific angular momentum, f) stagnation pressure.

trend reverses towards the tip of the blade. Consequence of the modification of the swirl angle at s4 is the off-design incidence of the stator LE. Moreover, extra turning is required from the inner sections of the OGV, leading to higher pressure losses (Fig. 16).

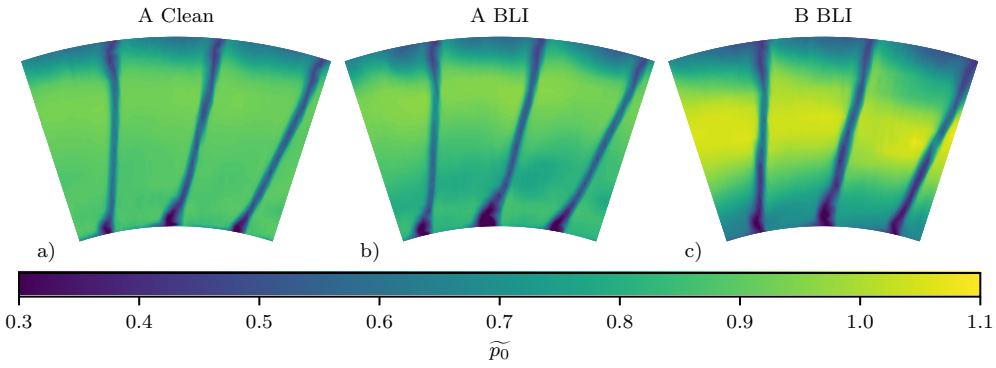

Figure 16. Measured contours of stagnation pressure downstream of the OGV - a) fan A Clean, b) fan A BLI, c) fan B BLI.

Absolute swirl, axial velocity, and work input can be related using the Euler equation (Eq. 1). Assuming axial inlet velocity, it can be rewritten as $\Delta h_0/U_{mid}^2 \approx \widetilde{r_4 V_{\theta 4}} =$

Table 2
Experimental measurements of the aerodynamic performance of fan A and B.

	A Clean	A BLI	B BLI
Flow coefficient ϕ	0.69	0.69	0.69
Stage loading coefficient Ψ	0.51	0.49	0.51
Rotor pressure rise coefficient ψ_{tt4}	0.89	0.85	0.88
Stage pressure rise coefficient ψ_{tt5}	0.86	0.82	0.85

$(U_4/U_{mid})\widetilde{V_{x4}}\sin\alpha_4$. Below 20% span swirl angle dominates loading up the blade (Fig. 15(e)), at 20% span the effects of axial velocity and swirl cancel out. From 20 to 60% span the drop in axial velocity dominates unloading the blade. Above 60% span the swirl angle becomes the most relevant again reducing the work input.

Blade loading is directly linked to the pressure rise generated by the blade. The increase in load in the inner sections (0-20% span) results in a larger rise in stagnation pressure as shown in Fig. 15(f) at s4. The rest of the rotor blade is unloaded, lowering the pressure rise. A large loss in stagnation pressure at s5 near the stator hub is observed in Fig. 15(f), this is attributed to the larger size of the OGV hub corner separation presented in (Fig. 16).

The flow phenomena presented in the previous paragraphs can be translated into changes in the global performance characteristics of fan A. The reduction in blade loading observed across most of the span results in a drop in stage loading coefficient Ψ, as shown in Table 2. The reduced loading along with the off-design incidence results in a further drop in rotor and stage pressure rise coefficients.

Experimental comparision of fans A and B

Reduced flow redistribution is observed for fan B than fan A between 0 and 20% span in Fig. 17(a). This leads to a more uniform mass flow distribution downstream of the rotor for fan A. This is confirmed in Fig. 17(d) by the lower radial angles associated with fan A at s3. For fan B, the mass flow migrates towards the midspan region as shown in Fig. 17(a). The flow for fan B further migrates downwards across the stator as suggested by the smaller radial angles at s4.

Despite the small difference in velocity near the hub at the fan face, the relative swirl angle across the span at s3 is essentially the same. Fig. 17(b) presents the relative swirl angle along with the LE metal angles of both designs. The realigment of the LE of fan B for optimum incidence can be observed. Additionally, the attempt to generate negative incidence near the tip is shown.

Following the realignment of the LE, the blade is recambered to deliver the desired work input. The amount of turning carried out by fan B is increased between 10 and 90% span. In contrast, a slight reduction in swirl angle at the tip is identified (Fig. 17(c)). The first effect of the larger swirl angle is the extra turning required from the stator to release the flow axially. The extra turning is required at midspan, which could be achieved by considering an OGV redesign with improved efficiency.

A large increase in specific angular momentum is observed in Fig. 17(e) between 20 and 80% span. This demonstrates that the midspan loaded design intent has been successfully

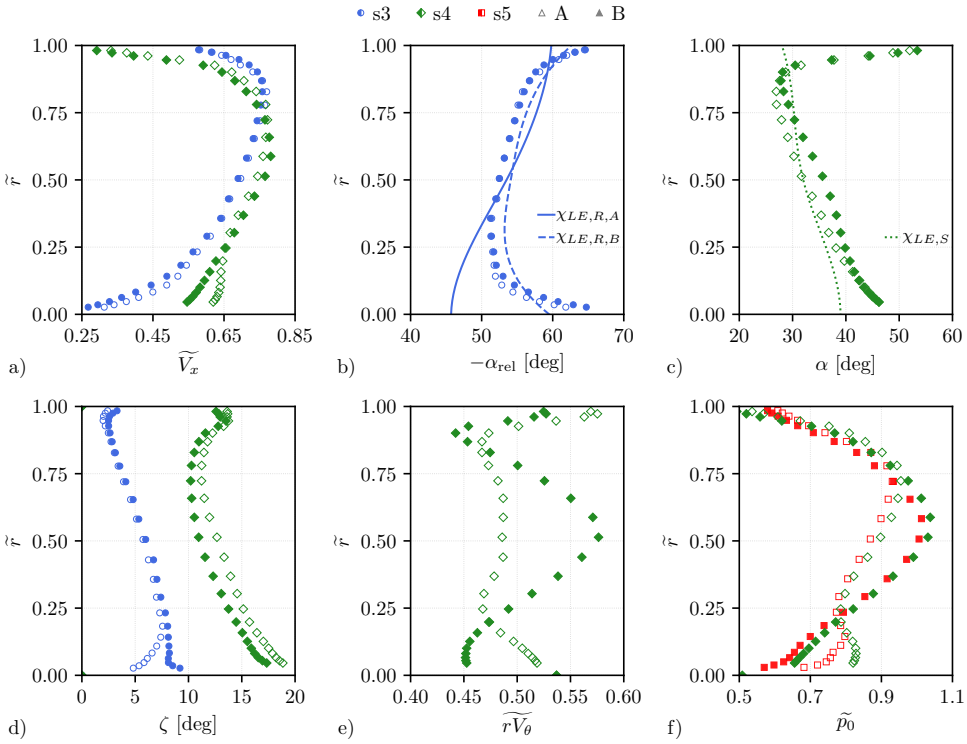

Figure 17. Measured spanwise distribution of fans A and B in BLI flow - a) relative swirl angle, b) absolute swirl angle, c) radial angle, d) axial velocity, e) specific angular momentum, f) stagnation pressure.

achieved. Near the tip, the combination of reduced axial velocity and swirl angle results in the desired unloaded tip.

The spanwise loading relates to the stagnation pressure rise distribution of rotor blade. Fan B is able to generate a much larger pressure rise at midspan than fan A, whilst maintaining lower values next to the hub and tip (Fig. 17(f)). A reduction in the OGV pressure losses near the hub can be identified as well in Fig. 17(f) for fan B. This can be associated with flow redistribution which takes place across the stator for fan B, easing the operation of the hub sections of the stator blade. This is confirmed in Fig. 16 by the smaller size of the hub corner separations.

Table 2 shows that fan B is able to recover the performance lost by fan A due to BLI. The work transferred to the flow (Ψ) is the same for fan B with BLI as it is for fan A in clean flow. The rotor and stage pressure rise for fan B with BLI is significantly higher than for fan A with BLI and almost as high as fan A in clean flow.

5.0 CONCLUSIONS

1. A low-speed fan rig for the experimental testing of BLI fuselage fans has been successfully demonstrated for two fan designs.
2. A conventional free-vortex fan design has been designed, manufactured, and tested for

clean and BLI inflow conditions.

3. The effect of the ingestion of radial BLI distortion on the free-vortex fan has been analysed:
   (a) Redistribution of the flow towards the low total pressure region near the hub is observed.
   (b) The inner blade sections operate at high incidence and increased work load whereas the tip produces reduced work with negative incidence.
   (c) The overall effect of BLI is the reduction in work loading input and efficiency.
4. A fan design optimised for aft-section fuselage BLI has been produced by:
   (a) Realigning optimally the leading edge metal angle to the inflow.
   (b) Loading the midspan whilst unloading the hub and tip sections.
   (c) Controlling the diffusion factor through custom work and chord distribution.
   (d) Increasing the operating range of the tip sections.
5. The new design better deals with the non-uniformity of the flow. It gives improved flow though the hub and restores the work input in the optimum blade sections, increasing the operating range.
6. The new fan design operating in BLI distortion gives increased overall work input and pressure rise relative to the conventional free-vortex design.

ACKNOWLEDGEMENTS

This research is part of the CENTRELINE project, which has received funding from the European Union's Horizon 2020 research and innovation programme under Grant Agreement No. 723242. The authors are grateful to Turbostream for the use of their solver. At the Whittle Laboratory, Phoenix Tse and James Taylor are thanked their technical advice, comments, and suggestions. Elliot Reed and Josh Firman are also thanked for their technical support manufacturing and assembling the rig.

NOMENCLATURE

Roman Symbols

c	Blade chord
C_p	Pressure coefficient
h	Enthalpy
i	Incidence angle
p	Pressure
r	Radius, Radial coordinate
T	Temperature
U	Rotor blade speed
V	Velocity
α	Swirl flow angle
ζ	Radial flow angle
θ	Circumferential coordinate

ρ	Density
χ	Blade metal angle

Non-dimensional Groups

$\widetilde{P}$	Static pressure = $2\left(P - \overline{P_{01}}\right)/\rho U_{\text{mid}}^2$
$\widetilde{P_0}$	Stagnation pressure = $2\left(P_0 - \overline{P_{01}}\right)/\rho U_{\text{mid}}^2$
$\widetilde{r}$	Span fraction = $(r - r_{\text{hub}})\,/\left(r_{\text{casing}} - r_{\text{hub}}\right)$
$\widetilde{rV_\theta}$	Specific angular momentum = $rV_\theta/r_{mid}U_{\text{mid}}$
$\widetilde{V_x}$	Axial velocity = V_x/U_{mid}
η_{ttx}	Total to total isentropic efficiency $\approx (\overline{p_{0x}} - \overline{p_{03}})/\rho U_{\text{mid}}^2 \left(\overline{r_4\widetilde{V}_{\theta 4}} - \overline{r_3\widetilde{V}_{\theta 3}}\right)$
ϕ	Flow coefficient = $\dot{m}/\rho A U_{\text{mid}}$
ψ_{ttx}	Total to total pressure rise coefficient= $2\,(\overline{p_{0x}} - \overline{p_{03}})/\rho U_{\text{mid}}^2$
Ψ	Stage loading coefficient = $\left(\overline{h_{04}} - \overline{h_{03}}\right)/U_{\text{mid}}^2 \approx \overline{r_4\widetilde{V}_{\theta 4}} - \overline{r_3\widetilde{V}_{\theta 3}}$

Subscripts

0	Stagnation quantity
1	Value just downstream of gauze
3	Value at rotor inlet
4	Value at rotor outlet
5	Value at OGV outlet
mid	Value at midspan
rel	Relative reference frame quantity
x	Axial component
θ	Circumferential component

Acronyms

BLI	Boundary layer ingesting
CFD	Computational fluid dinamics
DF	Lieblein diffusion factor
EXP	Experiment
LE	Leading edge
OGV	Outlet guide vane
TE	Trailing edge
VTP	Vertical tail plane

REFERENCES

1. Seitz, A., Peter, F., Bijewitz, J., Habermann, A., Goraj, Z., Kowalski, M., Castillo Pardo, A., Hall, C. A., Meller, F., Merkler, R., Petit, O., Samuelsson, S., Della Corte, B., van Sluis, M., Wortmann, G., and Dietz, M., "Concept Validation Study for Fuselage Wake Filling Propulsion Integration," *31st Congress of the International Council of the Aeronautical Sciences*, International Council of Aeronautical Sciences, Sept. 2018.

2. Hall, C. A., Schwartz, E., and Hileman, J. I., "Assessment of Technologies for the Silent Aircraft Initiative," *Journal of Propulsion and Power*, Vol. 25, No. 6, 2009, pp. 1153–1162.

3. Uranga, A., Drela, M., Greitzer, E., Titchener, N., Lieu, M., Siu, N., Huang, A., Gatlin, G. M., and Hannon, J., "Preliminary Experimental Assessment of the Boundary Layer Ingestion Benefit for the D8 Aircraft," *Proceedings of the 52nd AIAA Aerospace Sciences Meeting*, American Institute of Aeronautics and Astronautics, Jan. 2014, p. 0906.

4. Sandercock, D. M. and Sanger, N. L., "Some Observations of the Effects of Radial Distortions on Performance of a Transonic Rotating Blade Row," Technical Note NASA TN D-7824, National Aeronautics and Space Adminisitration, Dec. 1974.

5. Schmidt, J. F. and Ruggeri, R. S., "Performance with and without Inlet Radial Distortion of a Transonic Fan Stage Designed for Reduced Loading in the Tip Region," Technical Paper NASA TP 1294, National Aeronautics and Space Administration, Aug. 1978.

6. Sanger, N. L., "Effect of Rotor Meridional Velocity Ratio on Response to Inlet Radial and Circumferential Distortion," Technical Paper NASA TP 1278, National Aeronautics and Space Administration, July 1979.

7. Gunn, E. J. and Hall, C. A., "Aerodynamics of Boundary Layer Ingesting Fans," *Proceedings of the ASME Turbo Expo 2014*, No. GT2014-26142, American Society of Mechanical Engineers, June 2014.

8. Gunn, E. J., Tooze, S. E., Hall, C. A., and Colin, Y., "An Experimental Study of Loss Sources in a Fan Operating with Continuous Inlet Stagnation Pressure Distortion," *Journal of Turbomachinery*, Vol. 135, No. 5, 2013, pp. 051002.

9. Gunn, E. J. and Hall, C. A., "Non-Axisymmetric Stator Design for Boundary Layer Ingesting Fans," *Proceedings of the ASME Turbo Expo 2017*, No. GT2017-63082, American Society of Mechanical Engineers, June 2017.

10. Treaster, A. L. and Yocum, A. M., "The Calibration and Application of Five-Hole Probes," Tech. Rep. TM 78-19, Applied Research Laboratory, Jan. 1978.

11. van Sluis, M., Della Corte, B., and Rao, A. G., Personal communication, June 2018.

12. Brandvik, T. and Pullan, G., "An Accelerated 3D Navier-Stokes Solver for Flows in Turbomachines," *Journal of Turbomachinery*, Vol. 133, No. 2, 2011, pp. 021025.

13. Spalart, P. and Allmaras, S., "A One-equation Turbulence Model for Aerodynamic Flows," *Proceedings of the 30th aerospace sciences meeting and exhibit*, American Institute of Aeronautics and Astronautics, January 1992, p. 439.

14. NUMECA International, 2016, "Autogrid5," 2016, Accessed July 13, 2018.

15. Jerez Fidalgo, V., Hall, C. A., and Colin, Y., "A Study of Fan-Distortion Interaction Within the NASA Rotor 67 Transonic Stage," *Journal of Turbomachinery*, Vol. 134, No. 5, 2012, pp. 051011.

16. Lieblein, S., Schwenk, F. C., and Broderick, R. L., "Diffusion Factor for Estimating Losses and Limiting Blade Loadings in Axial-Flow-Compressor Blade Elements," Research Memorandum RM-E53D01, National Advisory Committee for Aaeronautics, June 1953.